Nucleic Acids Research, 2025, **53**, gkaf114
https://doi.org/10.1093/nar/gkaf114
Nucleic Acid Enzymes

Structural basis for aminoacylation of cellular modified tRNA^{Lys3} by human lysyl-tRNA synthetase

Swapnil C. Devarkar[1,*], Christina R. Budding[2], Chathuri Pathirage[2], Arundhati Kavoor[2], Cassandra Herbert[3], Patrick A. Limbach[3], Karin Musier-Forsyth[2,*], Yong Xiong[1,*]

[1]Department of Molecular Biophysics and Biochemistry, Yale University, New Haven, CT 06511, United States
[2]Department of Chemistry and Biochemistry, Center for RNA Biology, and Center for Retrovirus Research, Ohio State University, Columbus, OH 43210, United States
[3]Rieveschl Laboratories for Mass Spectrometry, Department of Chemistry, University of Cincinnati, Cincinnati, OH 45221, United States

[*]To whom correspondence should be addressed: Email: swapnilchandrakant.devarkar@yale.edu
Correspondence may also be addressed to Karin Musier-Forsyth. Email: musier@chemistry.ohio-state.edu
Correspondence may also be addressed to Yong Xiong. Email: yong.xiong@yale.edu

Abstract

The average eukaryotic transfer ribonucleic acid (tRNA) contains 13 post-transcriptional modifications; however, their functional impact is largely unknown. Our understanding of the complex tRNA aminoacylation machinery in metazoans also remains limited. Herein, using a series of high-resolution cryo-electron microscopy (cryo-EM) structures, we provide the mechanistic basis for recognition and aminoacylation of fully modified cellular tRNA^{Lys3} by human lysyl-tRNA synthetase (h-LysRS). The tRNA^{Lys3} anticodon loop modifications S34 (mcm^{5}s^{2}U) and R37 (ms^{2}t^{6}A) play an integral role in recognition by h-LysRS. Modifications in the T-, variable-, and D-loops of tRNA^{Lys3} are critical for ordering the metazoan-specific N-terminal domain of LysRS. The two catalytic steps of tRNA^{Lys3} aminoacylation are structurally ordered; docking of the 3′-CCA end in the active site cannot proceed until the lysyl–adenylate intermediate is formed and the pyrophosphate byproduct is released. Association of the h-LysRS–tRNA^{Lys3} complex with a multi-tRNA synthetase complex-derived peptide shifts the equilibrium toward the 3′-CCA end "docked" conformation and allosterically increases h-LysRS catalytic efficiency. The insights presented here have broad implications for understanding the role of tRNA modifications in protein synthesis, the human aminoacylation machinery, and the growing catalog of metabolic and neurological diseases linked to it.

Graphical abstract

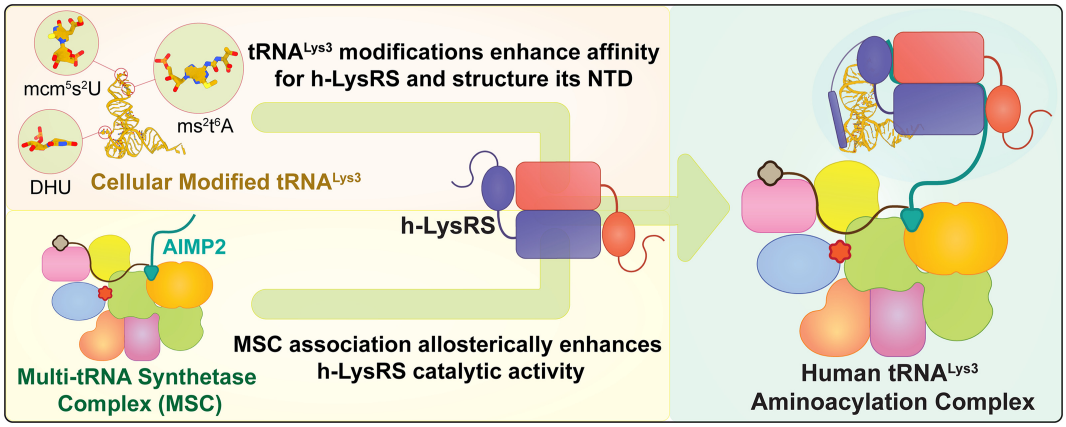

Introduction

Transfer ribonucleic acids (tRNAs) are essential noncoding adaptor RNA molecules that mediate the fidelity of messenger RNA (mRNA) translation across all living organisms [1]. Amino acids (aa) required for protein synthesis are delivered to the ribosome by aminoacylated or "charged" tRNAs, activated forms of tRNAs wherein the 3′-end is conjugated with a cognate aa by specialized enzymes called aminoacyl-tRNA synthetases (AARS) [2]. Almost all organisms encode at least 20 AARS, one for each aa, whereas higher eukaryotes encode a distinct set of mitochondrial and cytosolic AARS [3, 4]. Only two human (h) AARS have their mitochondrial and cytosolic isoforms encoded by the same gene, lysyl-tRNA synthetase (LysRS) and glycyl-tRNA synthetase, produced by alternative splicing [5] and alternate translation initiation sites, respectively [6, 7]. In most organisms, LysRS belongs to the class IIb subfamily of AARS and is evolutionarily and structurally related to aspartyl-tRNA synthetase (AspRS) and

Received: December 2, 2024. **Revised:** February 1, 2025. **Editorial Decision:** February 3, 2025. **Accepted:** February 6, 2025

asparaginyl-tRNA synthetase (AsnRS) [8, 9]. All class II synthetases possess oligomeric structures (dimers or tetramers) and contain three highly conserved active site motifs [10]. Motif 1 makes up the dimer interface and motifs 2 and 3 make up the aminoacylation active site, a seven-stranded b-sheet structure. In contrast to its bacterial counterpart, h-LysRS has a 70 aa N-terminal domain (NTD) that facilitates tRNA binding [11], but the structural basis of its role in aminoacylation remains unresolved. In metazoans, almost half of all cytosolic AARS and three scaffold proteins called "aminoacyl-tRNA synthetase complex interacting multifunctional proteins" (AIMP) assemble to form the multi-tRNA synthetase complex (MSC) (Fig. 1A) [12–14]. The exact architecture of the MSC and its regulatory role in aminoacylation remains controversial [14, 15]. h-LysRS is associated with the MSC via an interaction with AIMP2 (p38) and is released from the MSC after phosphorylation at S207 [16, 17]. pS207–LysRS is a regulator of nuclear transcription through synthesis of the dinucleotide Ap4A and is inactive for $tRNA^{Lys}$ aminoacylation [18, 19].

Another layer of complexity in higher eukaryotes is the extensive repertoire of RNA modifications observed in tRNAs, with an average of 17% of tRNA bases being modified post-transcriptionally in humans [20, 21]. $tRNA^{Lys3}$ (UUU), a major species of $tRNA^{Lys}$ in humans, carries two RNA modifications in its anticodon loop: 5-methoxycarbonylmethyl-2-thiouridine (mcm^5s^2U) on base 34 (S34) and 2-methylthio-N6-threonylcarbamoyladenosine (ms^2t^6A) on base 37 (R37) [22]. These modifications have been shown to regulate codon–anticodon wobble base-pairing and ribosomal frameshifting [23–25]. $tRNA^{Lys3}$ also carries an array of RNA modifications in the D-loop, T-loop, and variable loop regions that govern RNA folding and stability [20, 22, 26, 27]. However, the exact role of these modifications in recognition and aminoacylation by h-LysRS remains unknown.

Mutations in the cellular aminoacylation and RNA modification machineries have been linked to a growing number of neurodegenerative and metabolic disorders [4, 28–30]. h-LysRS has been implicated in Charcot–Marie–Tooth disease [31] and congenital leukoencephalopathy [32], whereas mutations in enzymatic machinery carrying out the ms^2t^6A modification on $tRNA^{Lys3}$ are linked to type II diabetes [33] and Galloway–Mowat syndrome [34]. $tRNA^{Lys3}$ also serves as the primer for HIV-1 reverse transcription, and the packaging of the h-LysRS–$tRNA^{Lys3}$ complex is an indispensable step in the HIV-1 lifecycle [35]. Structural studies on h-LysRS have been limited to crystallization and nuclear magnetic resonance (NMR) studies of its apo-form, often using truncated versions of the protein with the NTD missing in all the structures reported to date [9, 16, 36]. The only available structural information on the LysRS–$tRNA^{Lys}$ complex comes from a *Thermus thermophilus* LysRS–$tRNA^{Lys\ (UUU)}$ complex [37]. However, in this structure, only the anticodon stem–loop of bacterial $tRNA^{Lys}$ was resolved in complex with the anticodon-binding domain (ABD); how LysRS interacts with the acceptor stem and the 3′-CCA end remains unknown. Furthermore, bacterial LysRS lacks the NTD of h-LysRS and $tRNA^{Lys3}$ in humans is more extensively modified compared to its bacterial counterpart. Thus, the structural and mechanistic basis for $tRNA^{Lys3}$ recognition and aminoacylation by h-LysRS remains elusive.

To address these fundamental gaps in our understanding of $tRNA^{Lys3}$ recognition by h-LysRS and the role of $tRNA^{Lys3}$ modifications and the MSC in aminoacylation, we carried out a comprehensive structural and enzymatic characterization of h-LysRS complexed with cellular modified $tRNA^{Lys3}$ and the MSC scaffold protein AIMP2. Our results provide a structural and mechanistic basis for $tRNA^{Lys3}$ specificity of h-LysRS and the conformational landscape of the LysRS catalytic pathway. A comparison of h-LysRS complexes with cellular modified $tRNA^{Lys3}$ and *in vitro* transcribed (IVT) $tRNA^{Lys3}$ (unmodified) revealed how $tRNA^{Lys3}$ modifications are directly involved in recognition by h-LysRS and how the absence of these modifications compromises recognition. Strikingly, two steps in the h-LysRS aminoacylation reaction are ordered structurally, wherein the 3′-CCA end docking in the active site cannot proceed until the ATP hydrolysis-driven L-lysyl adenylate intermediate is formed and the resulting pyrophosphate moiety is released. AIMP2, which anchors h-LysRS to the MSC, allosterically enhances the catalytic efficiency of h-LysRS by driving the equilibrium of the h-LysRS–$tRNA^{Lys3}$ complex toward the 3′-CCA-end "docked" conformation. The detailed mechanistic and structural insights into $tRNA^{Lys3}$ aminoacylation by h-LysRS and the role of tRNA modifications and the MSC have broad implications for understanding the aminoacylation machinery in humans and the growing number of neurological and metabolic disorders linked to it.

Materials and methods

Expression and purification of wt and S207D LysRS

Full-length LysRS (wt and S207D) was cloned into pET11a protein expression vector with an N-terminal 6×-His affinity tag and recombinantly expressed in *Escherichia coli* BL21 (DE3) cell line. Cells were grown in Terrific Broth to an O.D. of 0.7–0.8 and then induced with 0.4 mM isopropyl β-D-1-thiogalactopyranoside (IPTG) at 18°C for 16 h. Cells were harvested via centrifugation, resuspended in lysis buffer [50 mM Tris–Cl, pH 7.5, 500 mM NaCl, 5% glycerol (v/v), 0.5 mM TCEP (tris (2-carboxyethyl)phosphine), and protease inhibitor cocktail tablets at 4°C], and subsequently lysed using a microfluidizer. The lysate was clarified by centrifugation to remove bacterial cell debris, and the supernatant was subjected to polyethyleneimine (PEI) precipitation at 0.45% (w/v) to remove contaminating nucleic acids. The supernatant from the PEI precipitation step was then used for ammonium sulfate precipitation (55% saturation) to separate the protein fraction from the contaminants. Pellets from ammonium sulfate precipitation were then solubilized in Buffer A [50 mM Tris–Cl, pH 7.5, 300 mM NaCl, 5% glycerol (v/v), and 0.5 mM TCEP at 4°C] and applied to a Ni-NTA resin packed in a gravity-flow column. The column was washed extensively with Buffer A containing 20 mM imidazole and then 6×-His tagged LysRS was eluted using Buffer A containing 400 mM imidazole. Eluted protein was dialyzed overnight into Buffer B [10 mM potassium phosphate, pH 7.5, 150 mM KCl, 5% glycerol (v/v), and 0.2 mM TCEP at 4°C]. Dialyzed eluate from Ni-NTA column was then applied to a hydroxyapatite column (Bio-Rad) and subjected to a gradient of increasing phosphate concentration [Buffer C: 400 mM potassium phosphate, pH 7.5, 150 mM KCl, 5% glycerol (v/v), and 0.2 mM TCEP at 4°C] to further enrich the LysRS fraction. Peaks from the hydroxyapatite column run were run on an SDS–PAGE gel, and fractions containing LysRS with purity >95% were then pooled and dialyzed into protein storage Buffer D

[50 mM HEPES, pH 7.5, 150 mM NaCl, 5% glycerol (v/v), and 0.2 mM TCEP]. Purified LysRS was then concentrated using Amicon® Ultra-15 Centrifugal Filter Concentrators with a 10 kDa cutoff, aliquoted, flash frozen in liquid nitrogen, and stored at −80°C.

Purification of cellular modified tRNA^{Lys3}

The protocol to purify fully modified human tRNA^{Lys3} using an affinity-capture-based method was adapted from Drino *et al.* [38]. HEK293T (ATCC) or Jurkat cell lines (NIH AIDS Reagent Program) were cultured at 5% CO_2 in 10% FBS (v/v) and 5% penicillin/streptomycin (Gibco) supplemented Dulbecco's Modified Eagle Medium (DMEM) or Roswell Park Memorial Institute (RPMI) medium (Gibco), respectively. Cells were washed with phosphate-buffered saline (PBS) (Thermo Fisher Scientific) and lysed with TRIzol (Invitrogen) per the manufacturer's instructions. The total cellular RNA was extracted with chloroform by centrifuging at 16 000 × *g* for 15 min at 4°C, and the aqueous layer was transferred to a fresh tube. LiCl stock solution (7.5 M) was added to the total RNA solution to a final concentration of 4 M, and the mixture was incubated overnight at –20°C, followed by centrifugation at 13 700 × *g* for 10 min at 4°C. This step allows for precipitation of high molecular weight RNA. The supernatant enriched for small RNAs was collected and ethanol precipitated with 2 µl of 5 mg/ml glycogen. The pellet was recovered and dissolved in 500 µl of ion exchange wash buffer (20 mM Tris, pH 7.5, 10 mM KCl, 1.5 mM $MgCl_2$, and 50 mM NaCl). The sample was loaded onto a HiTrap Q FF anion exchange column (5 ml) (Cytiva) on an ÄKTA pure chromatography system (Cytiva) equilibrated with the same buffer. RNA was eluted using a NaCl gradient from 10 to 1000 mM at a flow rate of 0.3–0.5 ml/min. Fractions eluting between 400 and 600 mM NaCl were collected and immediately precipitated with isopropanol at −20°C and dissolved in milliQ-H_2O.

A human tRNA^{Lys3}-specific affinity column was generated by coupling a 5′ amino-modified DNA oligonucleotide complementary to the 5′ 36 nt of tRNA^{Lys3} (5′ AAAAGTCTGATGCTCTACCGACTGAGCTATCCGGGC 3′) purchased from IDT to a HiTrap NHS-activated HP column (1 ml) (Cytiva) through a stable amide linkage as described [38]. Briefly, the affinity oligonucleotide stock solution was ethanol precipitated and dissolved in 1 ml of coupling buffer (0.2 M $NaHCO_3$ and 0.5 M NaCl, pH 8.3). The NHS-activated HP column was washed with 2 ml of 1 mM ice-cold HCl three times at a maximum flow rate of 0.5 ml/min. The oligonucleotide solution was immediately injected onto the column, and the column was sealed and incubated for 30 min at 25°C (or 4 h at 4°C). Uncoupled activated groups were deactivated and unbound oligonucleotides were removed by repeated washings with washing buffer A (0.5 M ethanolamine and 0.5 M NaCl, pH 8.3) and washing buffer B (0.1 M NaOAc and 0.5 M NaCl, pH 4). The coupling efficiency of the oligonucleotide to the column was ∼40%, and the column was stored in 0.05 M Na_2HPO_4 and 0.1% NaN_3, pH 7 at 4°C.

To capture human tRNA^{Lys3}, the small RNA pool was denatured by incubation at 75°C for 3 min, followed by snap-cooling on ice. The RNA was mixed with 20 ml of pre-cooled binding buffer (30 mM HEPES-KOH, pH 7.0, 1.2 M NaCl, and 10 mM $MgCl_2$). The affinity column was equilibrated with the binding buffer, and the binding of tRNA to the column was performed under controlled temperature conditions—the RNA pool was circulated through the affinity column for 90 min at 65°C, and then the temperature was gradually decreased to 40°C over a 3–4 h period. The column was washed with 10 ml of 2.5 mM HEPES-KOH, pH 7.0, 0.1 M NaCl, and 10 mM $MgCl_2$ at 40°C. Finally, tRNA^{Lys3} was eluted from the column with 0.5 mM HEPES-KOH, pH 7.0, and 1 mM EDTA at 75°C. The eluted RNA was immediately ethanol precipitated, and the purified tRNA^{Lys3} was checked on a 10% denaturing polyacrylamide gel. The yield of modified human tRNA^{Lys3} starting with ∼100 million HEK 293T cells was ∼5 µg.

LC-MS validation of tRNA^{Lys3} modifications

To detect tRNA^{Lys3} modifications, liquid chromatography tandem mass spectrometry (LC-MS/MS) was performed. The RNA sample was digested using 50 U/µg of commercially purchased RNase T1 (Worthington Biochemical, Lakewood, NJ) in 110 mM ammonium acetate at 37°C for 1.5 h. The enzymatic digestion products were separated using a Dionex Ultimate 3000 (Thermo Scientific) UHPLC system equipped with an Xbridge BEH C18 column (2.1 mm × 150 mm, 2.5 µm, Waters) using ion-pair reverse phase liquid chromatography (IP-RPLC). Mobile phases were 8 mM triethylamine (TEA) and 200 mM hexafluoroisoproponal (HFIP) in water (mobile phase A: MPA) and 8 mM TEA and 200 mM HFIP in 50:50 water: methanol (mobile phase B: MPB). The IP-RPLC gradient profile was 5% MPB until 5 min followed by a linear ramp to 73% MPB at 40 min. The column was flushed with 100% MPB for 5 min and re-equilibrated for 15 min at 5% MPB. The flow rate was 80 µl/min with a column temperature of 60°C.

An LTQ-XL linear ion trap mass spectrometer (Thermo Fisher Scientific) was used to detect the resolved digestion products in negative polarity mode. Electrospray ionization conditions were as follows: capillary temperature 375°C, capillary voltage of −30 V, spray voltage of 3.7 kV and 35, 20, and 20 arbitrary flow units of sheath, auxiliary, and sweep gas, respectively. Data were acquired with the range of m/z 600–2000; MS/MS scans were collected through data-dependent acquisition of the four most abundant MS ions. The maximum injection was fixed at 250 ms with an AGC cutoff of 500 counts. LC-MS/MS data analysis was performed using RNAModMapper (RAMM) [39, 40] and Xcalibur v4.1. (Thermo Fisher Scientific). All expected RNase T1 digestion products from human tRNA^{Lys3} were detected in the mass spectral data and could be mapped to the tRNA sequence (Supplementary Fig. S1A and Supplementary Table S1). These digestion products included the known modifications on human tRNA^{Lys3}, N^2-methylguanosine at position 10 (m^2G10), dihydrouridine at positions 16 and 20 (D16 and D20), 5-methoxycarbonylmethyl-2-thiouridine at position 34 (mcm^5s^2U34), 2-methylthio-N^6-threonylcarbamoyladenosine at position 37 (ms^2t^6A37), N^7-methylguanosince at position 46 (m^7G46), 5-methylcytidine at position 49 (m^5C49), 5,2′-O-dimethyluridine at position 54 (T^m54), and 1-methyladenosine at position 58 (m^1A58). Automated analysis of MS/MS fragmentation data by RAMM [40] confirmed the sequences of all digestion products except the fully modified anticodon sequence "ACU[mcm^5s^2U]UU[ms^2t^6A]AYCUGp" and the variable loop digestion product "[m^7G]U[m^5C][m^5C]AGp." These

two fragments were analyzed and verified manually. One limitation of the mass spectrometry-based approach is that uridine and pseudouridine cannot be differentiated. Thus, the presence of pseudouridine at positions 27, 39, and 55 (ψ27, ψ39, and ψ55) was not confirmed by LC-MS. Overall, the LC-MS analysis identified nine RNA modifications including anticodon loop modifications known to be present in human $tRNA^{Lys3}$ in the purified tRNA sample.

In vitro transcription of $tRNA^{Lys3}$

Human $tRNA^{Lys3}$ was IVT by in-house purified T7 RNA polymerase [41] prepared using plasmid p6XHis-T7 (P266L) [42], a gift from Anna Pyle (Addgene plasmid #174866). The plasmid template used for transcription (pIDTSmart-htRNALys3) [43] was digested with FokI followed by buffered phenol–chloroform extraction and ethanol precipitation [44]. Transcription reactions (4 ml) containing 240 μg linearized plasmid template or polymerase chain reaction (PCR) product from a 1-ml PCR reaction were performed in 80 mM HEPES, pH 8, 30 mM Mg $(OAc)_2$, 10 mM dithiothreitol (DTT), 5 mM spermidine, 0.01% Triton-X-100, 4% PEG8000, 0.5 mg/ml bovine serum albumin (BSA), 4 mM of each ribonucleotide triphosphate (rNTP), 10 μg/ml pyrophosphatase, and an optimized amount of recombinant P266L T7 RNA polymerase at 37°C for 5 h. The reaction was quenched with 50 mM EDTA, pH 8, and the tRNA was purified by acid–phenol chloroform extraction followed by anion exchange chromatography as described [45, 46]. Briefly, the tRNA product from a 4-ml transcription was loaded onto a 3-ml DEAE Sepharose Fast Flow gravity column (Cytiva) equilibrated with 20 mM Tris–HCl, pH 8.0, 150 mM NaCl, and 5 mM $MgCl_2$ and washed with the same buffer containing 250 mM NaCl. Bound tRNA molecules were eluted from the column using 15 ml of 1 M NaCl buffer. Fractions containing the tRNA were identified by urea–PAGE, pooled, and ethanol precipitated. tRNAs were resuspended in MilliQ-H_2O and the purity was assessed by urea–PAGE.

Cryo-EM grid preparation and data collection

Purified wt LysRS was mixed with either cellular purified $tRNA^{Lys3}$ or IVT $tRNA^{Lys3}$ in a 1:1 stoichiometric ratio and a final concentration of 10 μM h-LysRS–$tRNA^{Lys3}$ along with 2.5 mM L-lysine and 2 mM of either AMP (adenosine monophosphate) or AMPCPP (α,β-methyleneadenosine-5′-triphosphate). For datasets containing AIMP2-N36, the chemically synthesized peptide was added to a final concentration of 100 μM. Complex formation was allowed to proceed for 60 min at 4°C. The assembled complex (4 μl) was applied to C-flat R2/1 holey carbon copper grids (EMS) after glow discharging the grids at 11 mA for 30 s (Pelco). Grids were blotted at blot force 1 for 6 s and plunge frozen in liquid ethane using the Vitrobot Mark IV system (Thermo Fisher Scientific) maintained at 10°C. The detergent CHAPSO (0.075% final concentration) was added just before grid freezing to ensure uniform ice thickness and particle distribution.

Grids were screened for optimal ice thickness and particle concentration. Data collection was carried out from a single screened grid using a 300 kV Titan Krios cryo-transmission electron microscope (Thermo Fisher Scientific) equipped with a K3 camera (Gatan) and an imaging energy filter (Gatan) operated at a slit width of 15 eV. The dataset was collected in counting super-resolution mode with a nominal magnification of ×81 000 leading to a physical pixel size of 1.07 Å (super-resolution pixel size is 0.535 Å). The data were collected at a dose rate of 15 e^-/pixel/s with a total electron dose of 50 $e^-/Å^2$ applied over 40 frames and a defocus range of −1.0 μm to −2.0 μm.

Cryo-EM data processing and model building

The cryo-EM data processing workflow was carried out using cryoSPARC v4 [47]. Movie frames were motion corrected using Patch motion correction and binned 2-fold to yield a stack of motion-corrected micrographs with a pixel size of 1.07 Å. These micrographs were then manually curated, and an initial round of particle picking was performed using Blob picker on a subset of 500 micrographs. A 2D classification job on these initial particle stack yielded ideal 2D templates that were used to perform template-based particle picking on the entire dataset. The particle stack from template picker was further curated to remove damaged/denatured particles using 2D classification. After 2D classification, selected particles were carried forward to *ab initio* reconstruction for generating three different volumes and used as 3D references for heterogeneous refinement of the particle stack. Particles corresponding to apo-LysRS, LysRS–$tRNA^{Lys3}$ undocked state, and LysRS–$tRNA^{Lys3}$ docked state were segregated and further refined using nonuniform (NU) refinement. These particle stacks were further curated using 3D classification to improve compositional and conformational homogeneity. The final particle stacks were then polished using reference-based motion correction and used for NU-refinement to create the final reconstructions. All datasets were processed as above, and the details are included in Supplementary Tables S2–S5. The final reconstructions were uploaded to the Electron Microscopy Data Bank (EMDB).

Model building was done in Coot [48] with a previously published model of human LysRS bound to AIMP2 peptide (PDB: 6ILD) and the crystal structure of mammalian $tRNA^{Lys3}$ (PDB: 1FIR) as the starting templates. After initial rigid-body docking, the $tRNA^{Lys3}$ and LysRS residues were manually fit into the high-resolution map using real-space refinement modules. Some regions of LysRS that were missing in the starting template were built *de novo* into the high-resolution map. Two rounds of real-space refinement in PHENIX [49] were carried out, and the outliers were manually corrected in Coot before deposition in the Protein Data Bank (PDB).

Aminoacylation assays

IVT or fully modified cellular $tRNA^{Lys3}$ was folded in 50 mM HEPES, pH 7.5, by heating at 80°C for 2 min, 60°C for 2 min, followed by the addition of 10 mM $MgCl_2$, incubation for 5 min at room temperature, and placement on ice. The active tRNA concentration was determined by aminoacylation assays as described below, with 1 μM LysRS and time points taken up to 40 min to ensure plateau-level charging.

AIMP2-N36 peptide [16] purchased from Biosynth was resuspended in 1 mM TCEP, 10% glycerol, and stored at −80°C. Concentration was determined by measuring the absorbance at 280 nm using an extinction coefficient of 5240 M^{-1} cm^{-1}. Aminoacylation assays for determination of kinetic parameters in the presence and absence of AIMP2-N36 peptide were performed as follows. LysRS was diluted to 200 nM in 50 mM HEPES, 0.1 mg/ml BSA, 20 mM

β-mercaptoethanol (βME), and 20 mM KCl with or without 50-fold molar excess AIMP2-N36 peptide and incubated on ice for ∼1 h prior to starting the reaction. Aminoacylation was conducted at 30°C in the presence of 0.08–10 μM active unmodified tRNA, refolded as described above, 0.1 mg/ml BSA, 20 mM KCl, 20 mM $MgCl_2$, 20 mM βME, 4 mM ATP, 50 mM HEPES, pH 7.4, 20 μM lysine, and 2.5 μM [^{3}H]lysine (60 Ci/mmol in 2% ethanol, American Radiolabeled Chemicals). Reactions were initiated with 10 nM LysRS. At 20-s time intervals out to 2 min, an aliquot (10 μl) of reaction mix was quenched on Whatman 3 mM filter pads presoaked with 5% trichloroacetic acid (TCA). Pads were washed with excess 5% ice-cold TCA three times for 20 min each, before drying and analysis by liquid scintillation counting. Specific activity was calculated with 1× reaction buffer (no washes) to calculate [^{3}H] counts per min per pmol lysine.

Electrophoretic mobility shift assays

Electrophoretic mobility shift assays (EMSAs) were conducted by incubating increasing concentrations of wt LysRS (0–5 μM) with 37.5 nM unmodified or modified tRNA^{Lys3} in binding buffer (20 mM HEPES, pH 7.4, 60 mM NaCl, 10 mM KCl, 1 mM $MgCl_2$, 400 μM DTT, and 8% glycerol) at room temperature for 30 min. Complexes were run on 4%–16% NativePAGE gels (Invitrogen) in a Tris–Borate native buffer (pH 8.3) for 2 h at 100V, stained with SYBRgold (Invitrogen), and imaged using Cy3 filters on an Amersham™ Typhoon™ RGB imager (Cytiva). Binding was quantified using ImageJ software, and the proportion of bound to total tRNA^{Lys3} was calculated. Dissociation constants (K_d) were calculated by plotting percent bound tRNA^{Lys3} versus LysRS concentration and fitting the data to the Hill equation [50] using GraphPad Prism software version 10.3.0 for MacOS.

Results

Structure of human LysRS-cellular modified tRNA^{Lys3}–AIMP2 complex

To gain a mechanistic and structural understanding of tRNA^{Lys3} recognition and aminoacylation by LysRS, we carried out cryo-EM studies of h-LysRS complexed with cellular modified tRNA^{Lys3} and the MSC adaptor protein, AIMP2. Fully modified tRNA^{Lys3} was purified from HEK293T or Jurkat cells (detailed protocols in "Materials and methods" section), and mass spectrometry analysis validated the presence of most of the previously reported modifications in the purified tRNA^{Lys3} sample (Supplementary Fig. S1A and B, and Supplementary Table S1) [22]. The LysRS interacting N-terminal region of AIMP2 (N36) was chemically synthesized and used in the cryo-EM studies [16]. Cellular modified tRNA^{Lys3} was complexed with recombinantly purified h-LysRS and AIMP2–N36 in the presence of adenosine monophosphate (AMP) and L-lysine for single-particle cryo-EM structural studies. A final reconstruction of dimeric LysRS bound to a single-modified tRNA^{Lys3} and two copies of AIMP2–N36 was resolved to 2.75 Å and used for model building (Fig. 1B and C, and Supplementary Fig. S1C–F, Supplementary Tables S2–S4).

The high-resolution cryo-EM reconstruction allowed for unambiguous modeling of majority of h-LysRS, AIMP2–N36, and all nucleotides of the cellular modified tRNA^{Lys3} (Fig. 1C, and Supplementary Fig. S2A and Supplementary Table S4). Consistent with the mass spectrometry analysis, tRNA^{Lys3} modifications exhibited distinct densities in the cryo-EM reconstruction (Fig. 1D). The only tRNA^{Lys3} modifications that cannot be confirmed by mass spectrometry analysis are pseudouridines (ψ) due to their identical mass to uridines. However, the H1N1 imino group of pseudouridine is a strong hydrogen bond donor and often leads to a water molecule being coordinated between its 5′-phosphate and H1N1 imino group [51, 52]. This molecular signature was used to confirm the presence of pseudouridine in the cellular modified tRNA^{Lys3} used in this study (Supplementary Fig. S2B). Nine different tRNA modifications and a total of 14 modified nucleotides were modeled for the cellular purified tRNA^{Lys3}.

The first ten residues of AIMP2 act as a latch, securing the dimeric interface formed by the ABD of one LysRS monomer with the aminoacylation domain (AAD) of the other and anchoring the LysRS–tRNA^{Lys3} complex to the MSC (Fig. 1E). Strikingly, the anticodon loop (U33-R37) is extensively remodeled by LysRS, compared to the crystal structure of tRNA^{Lys3} alone (PDB: 1FIR) [53] (Fig. 1F and G, and Supplementary Movie S1). All five bases in the anticodon loop are unstacked and form an extensive network of interactions with LysRS (Fig. 1G). Interestingly, U33 and R37, adjacent to the anticodon bases S34, U35, and U36, are also integral to the recognition of tRNA^{Lys3}. U33 forms base-specific salt bridges with K141 and N159 while stacking against the aliphatic sidechain of K141 and the guanidium group of R161. The RNA modifications on S34 (mcm^5s^2U) form specific interactions with the LysRS ABD, wherein R161 forms a salt bridge with the 5-mcm moiety and the 2-thiol modification stacks against T191 and the aliphatic sidechain of K193 (Fig. 1G). These interactions are further strengthened by hydrophobic packing interactions of S34 against L142, F144, and M157. U35 and U36 are recognized by LysRS ABD via base-specific ionic interactions as well as hydrophobic stacking interactions. F144 forms a three-ring stack with U35 and U36, which is further stabilized by salt bridges between R136, Q155, and E195 of LysRS ABD and U35 and U36 of tRNA^{Lys3}, respectively (Fig. 1G). The ms^2t^6A-modified base (R37) is recognized by the linker region (208–220) connecting the LysRS ABD to its AAD. H217 and F218 of this linker region stack against the adenine base and the bulky N6-threonylcarbomyl modification, whereas H215 forms hydrophobic stacking interaction with the 2-methylthio moiety of R37 (Fig. 1G). The hydrophobic stacking interactions of H215 and H217 are further strengthened by hydrogen bonding with the R37 phosphate backbone and the N6-threonylcarbomyl modification, respectively.

The NTD of LysRS (1-65) is unique to higher eukaryotes and, in the absence of tRNA^{Lys3}, is predicted to be unstructured [54]. The NTD of h-LysRS is either disordered or was deleted in all the X-ray crystallography structures reported to date [9, 16]. h-LysRS NTD is highly basic and has been proposed to play a role in tRNA binding and aminoacylation [11]. In the complex structure reported here, residues 14–43 of the NTD are clearly resolved in the cryo-EM reconstruction and form an extended α-helix that is anchored at the base of the tRNA^{Lys3} T-loop and runs along the anticodon arm of tRNA^{Lys3} (Fig. 2A, and Supplementary Fig. S2C and Supplementary Movie S2). All the basic residues of the N-terminal helix face tRNA^{Lys3}, creating a highly positive surface that mediates several key protein–RNA interactions

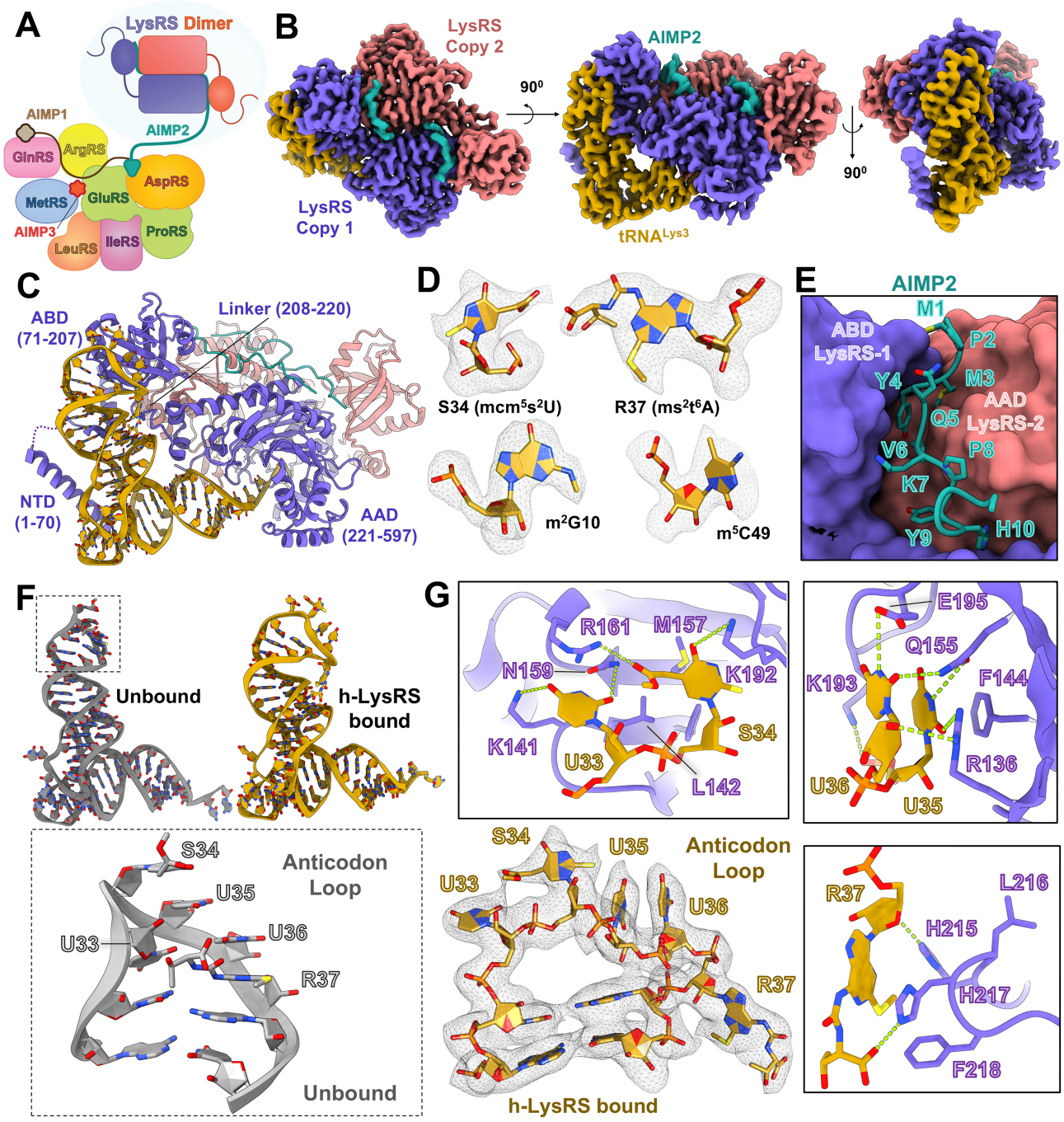

Figure 1. Structure of h-LysRS bound to modified cellular tRNA^{Lys3} and AIMP2. (**A**) A schematic representation of the MSC. h-LysRS dimer is anchored to the MSC by AIMP2 and is highlighted. (**B**) Cryo-EM reconstruction of wt h-LysRS bound to modified cellular tRNA^{Lys3} and AIMP2 in the presence of AMP and L-lysine. (**C**) Structural model built for the h-LysRS–tRNA^{Lys3}–AIMP2 complex based on the cryo-EM reconstruction shown in panel (B). The various domains of h-LysRS are highlighted. (**D**) Representative modified nucleotides in tRNA^{Lys3} are shown with the corresponding cryo-EM map density from the reconstruction shown in panel (B). (**E**) The N-terminal residues of AIMP2 (teal) secure the dimeric interface between the ABD of one LysRS monomer (purple) and the AAD of the other (coral orange) and are shown in stick representation. (**F**) Cellular modified tRNA^{Lys3} in the h-LysRS bound (gold) and unbound (gray) form is shown. The bottom inset shows the anticodon stem loop of cellular modified tRNA^{Lys3} in the unbound form (PDB: 1FIR), highlighting the stacking interactions between the five anticodon loop bases (U33-R37). (**G**) The anticodon loop of tRNA^{Lys3} (U33-R37) bound to h-LysRS is shown along with the corresponding cryo-EM map density. The insets highlight the interactions of the anticodon loop nucleotides (gold) with LysRS (purple).

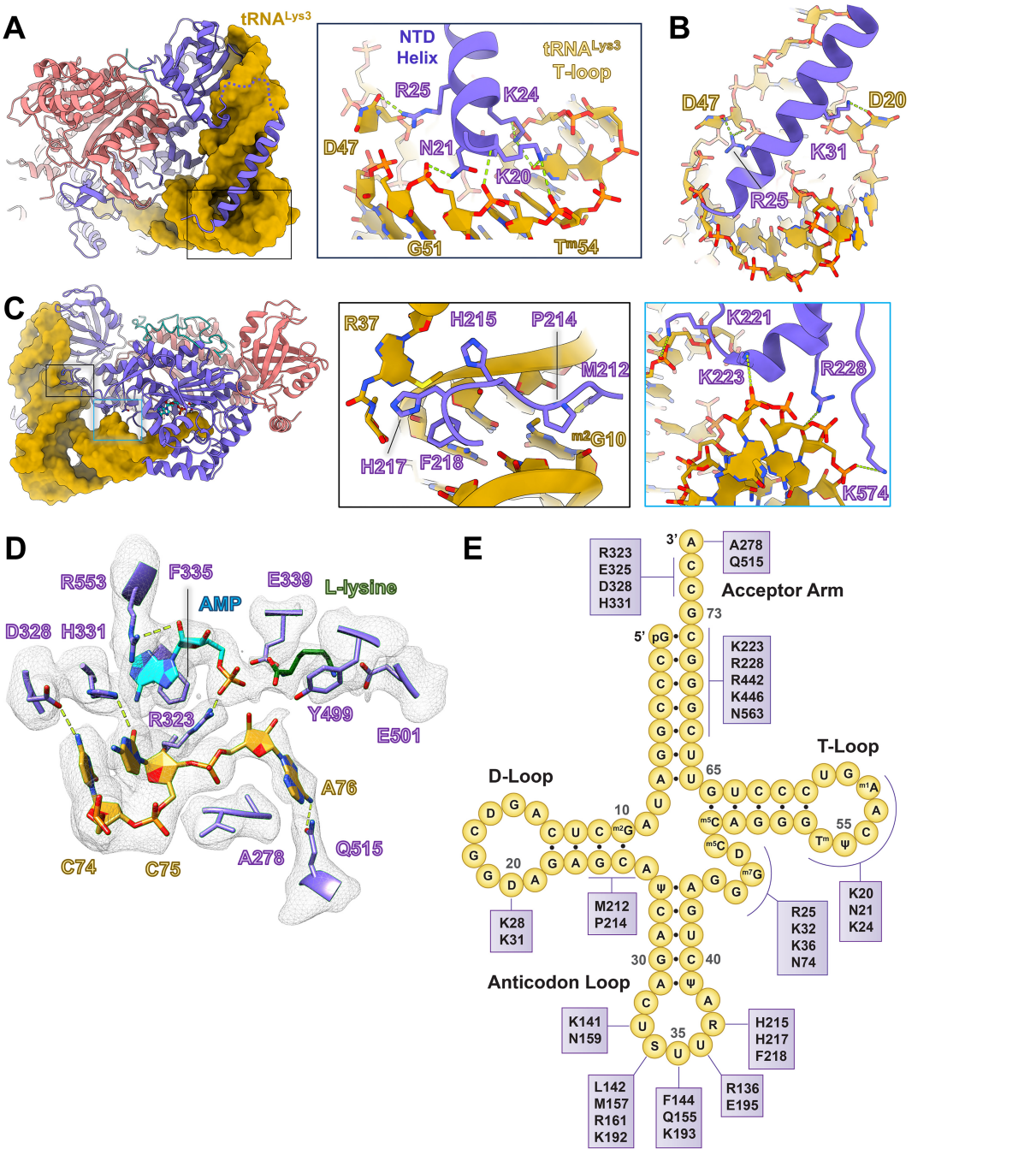

Figure 2. tRNA^{Lys3} interactions with h-LysRS NTD and active site. (**A**) A view of the h-LysRS–tRNA^{Lys3} complex (h-LysRS in cartoon and tRNA^{Lys3} in surface view) showing the NTD helix of LysRS interacting with the elbow region of tRNA^{Lys3}. The inset highlights the residues at the base of the NTD helix and their contacts in the tRNA^{Lys3} T-loop and variable loop. (**B**) A magnified view showing the N-terminal helix of h-LysRS and its interactions with two dihydrouridine bases of tRNA^{Lys3}, D20 and D47, of the D-loop and variable loop, respectively. (**C**) The docked state h-LysRS–tRNA^{Lys3} complex is shown, with the insets highlighting key interactions for docking the 3′-CCA end of tRNA^{Lys3}. LysRS linker residues interact with the D-arm (middle) whereas the acceptor arm is stabilized by a series of ionic interactions (right). (**D**) A magnified view of the h-LysRS active site is shown with the tRNA^{Lys3} 3′-CCA end docked in. The corresponding cryo-EM map density is shown in mesh. (**E**) The interaction map of the h-LysRS–tRNA^{Lys3} complex is shown with tRNA^{Lys3} portrayed in the conventional clover-leaf representation.

(Fig. 2A and B, and Supplementary Fig. S2D). Residues K20, at the N-terminus of the extended helix, N21, and K24 interact with the phosphate backbone of the T-loop. K20 and K24 also form ionic interactions with the modified nucleotide ψ55. In addition, K28, K32, and K36 interact with the phosphate backbone of the anticodon arm of tRNA^{Lys3}. Interestingly, two key RNA modifications in the D-loop and the variable loop play crucial roles in stabilizing the N-terminal helix. U20 of the D-loop and U47 of the variable loop are modified to 5,6-dihydrouridine (D), leading to a loss in the planar nature of these pyrimidine bases and their ability to stack against the tRNA^{Lys3} central core. In the structure reported here, D20 and D47 of tRNA^{Lys3} adopt an unstacked conformation, creating a wider groove between the D-loop and the variable loop and

allowing the NTD of h-LysRS to dock. D20 and D47 further stabilize the h-LysRS NTD by forming interactions with K31 and R25, respectively (Fig. 2B).

Similar to all class II AARS, the active site of h-LysRS is formed at the base of six antiparallel β-sheets and a seventh parallel β-sheet. The h-LysRS active site has three pockets, one for each of the substrates in the aminoacylation reaction—ATP, L-lysine, and the 3′-CCA end of the tRNA. The cellular modified $tRNA^{Lys3}$ in this reconstruction was present exclusively in the "docked" state, wherein the 3′-CCA end is inserted into the h-LysRS active site. The key interactions for positioning the acceptor arm toward the active site involve h-LysRS linker residues M212 and P214 that contact $tRNA^{Lys3}$ from the D-arm minor groove and form hydrophobic stacking interactions with 2-methyl guanosine (m^2G10) as well as F218 and K221 that form additional interactions with the D-arm (Fig. 2C). The acceptor arm is stabilized by interactions mediated by K223, E224, R228, R442, K446, and K574 (Fig. 2C). All three 3′-terminal residues of the tRNA form base-specific interactions with h-LysRS AAD (Fig. 2D). C74 and C75 of $tRNA^{Lys3}$ are recognized by h-LysRS motif 2 residues. The base of C74 forms a hydrogen-bonding network with E325, G326, and D328. In the active site, H331 coordinates C75 by forming base-specific interactions while simultaneously stacking against the adenine base of AMP. E325 and H331 are invariable motif 2 residues of LysRS conserved across prokaryotes and eukaryotes [55]. The 3′-terminal A76 base is unstacked relative to C75 and stabilized in a hydrophobic pocked formed by the "flipping loop" (272–282), located between motifs 1 and 2, and residues P471, L472, and F512. The flipped A76 base stacks on A278 and forms hydrogen bonds with Q515. This conformation of A76 places the 3′-hydroxyl group of the ribose near the α-phosphate of AMP and the α-carboxylic group of L-lysine. An alternate conformation for the A76 base (conformation B) was also observed in the cryo-EM reconstruction wherein the A76 base is rotated away from the active site and placed in an alternate hydrophobic pocket formed by A278, V279, F528, and I529 (Supplementary Fig. S2E). The functional relevance of this alternate A76-binding pocket in aminoacylation is not apparent but may have a role in Ap4A synthesis carried out by h-LysRS. Both conformations of the flipped A76 base are stabilized by hydrogen bonding between the amino group of A76 base and Q515 of h-LysRS. The extensive interaction network between h-LysRS and cellular modified $tRNA^{Lys3}$ is summarized in Fig. 2E.

The binding mode of ATP and L-lysine in the h-LysRS active site is highly conserved across species as well as within the class IIb family of AARS [9, 56]. The adenine base of AMP forms pi-stacking interactions with F335 and is further stabilized by R323 and R553 that form an "arginine tweezer," a highly conserved feature across class II AARSs [57]. The class II invariant motif 2 residue R323 coordinates the α-phosphate of AMP and is within hydrogen bonding distance from the 3′-hydroxyl of the A76 ribose. L-lysine is coordinated in the h-LysRS active site via a series of ionic and hydrophobic interactions. The aliphatic sidechain of L-lysine stacks in between Y341 and Y499 whereas the ε-amino group interacts with E501. E339 and E301 form ionic interactions with the α-amino group of L-lysine, placing its α-carboxylic group near the α-phosphate of AMP and the 3′-hydroxyl group of the A76 ribose (Fig. 2D).

ATP state governs 3′-CCA end docking of $tRNA^{Lys3}$ in the active site

To gain a mechanistic understanding of the aminoacylation pathway for $tRNA^{Lys3}$, we carried out cryo-EM studies of the h-LysRS–$tRNA^{Lys3}$ complex in the presence of L-lysine and either a nonhydrolyzable ATP analog, α,β-methylene-adenosine 5′-triphosphate (AMPCPP), or AMP to mimic the pre- and post-hydrolysis states of LysRS–$tRNA^{Lys3}$ complex, respectively. The $tRNA^{Lys3}$ used in these studies was produced by *in vitro* transcription (IVT), and therefore, lacked any RNA modifications. This allowed us to systematically study the effects of individual cellular $tRNA^{Lys3}$ modifications on the h-LysRS–$tRNA^{Lys3}$ complex. The AMP dataset yielded three distinct reconstructions: apo-LysRS, LysRS–$tRNA^{Lys3}$ complex in the "undocked" state, and h-LysRS–$tRNA^{Lys3}$ complex in the "docked" state (Fig. 3A and Supplementary Table S5). In contrast, the conformational state of the LysRS–$tRNA^{Lys3}$ complex in the AMPCPP dataset was exclusively in the "undocked" state (Fig. 3A and B). Compared to the "docked" state, the LysRS active site in the AMPCPP bound "undocked" state has notable differences. AMPCPP assumes a bent conformation in the LysRS active site, wherein the β- and γ-phosphate fold back toward the adenine base (Fig. 3B). The interactions of the adenine base of AMPCPP are similar to that observed in the docked state detailed above. Two magnesium ions were observed in the LysRS active site in the AMPCPP bound "undocked" state, coordinated by conserved residues E487 and E494, and play a key role in orienting the triphosphate moiety of ATP in the LysRS active site. In the presence of AMP, no discernable density attributable to magnesium ions was observed in the h-LysRS active site. This difference between the AMPCPP and AMP bound states of h-LysRS suggests that magnesium plays an active role in the first catalytic step of h-LysRS, ATP hydrolysis, and formation of the lysyl–adenylate intermediate but is not involved in the second step of catalysis.

To understand why the non-hydrolyzable ATP analog, AMPCPP, prevented the complex from assuming the "docked" state, we overlayed the structures for the docked and undocked states of the LysRS–$tRNA^{Lys3}$ complex. This comparison revealed that the β- and γ-phosphates of the ATP analog clash with the 3′-CCA end of $tRNA^{Lys3}$ in the LysRS active site (Fig. 3C). Interestingly, H331 directly interacts with the β-phosphate of AMPCPP in the undocked state, and this same residue is involved in forming base-specific interactions with C75 of $tRNA^{Lys3}$ in the docked state. Therefore, the docking of the 3′-CCA end of $tRNA^{Lys3}$ cannot proceed until the lysyl–adenylate intermediate is formed and the cleaved pyrophosphate moiety is released from the active site. This is in contrast to the previously reported crystal structures for the docked state of yeast AspRS (y-AspRS) [56], a closely related class IIb AARS. The 3′-CCA end docking for $tRNA^{Asp}$ in the y-AspRS active site was shown to be independent of the ATP state and it was postulated that the two steps in aminoacylation of $tRNA^{Asp}$ are not ordered. Comparing our "docked" state structure of the h-LysRS–$tRNA^{Lys3}$ with that of y-AspRS–$tRNA^{Asp}$ (PDB: 1ASZ) highlighted key differences in the active site architecture of these two enzymes. Compared to y-AspRS, the active site entrance in h-LysRS is narrower (Supplementary Fig. S3A) and is sterically blocked by the β- and γ-phosphate of ATP. h-LysRS encodes several insertions in the AAD (371–381, 388–396, and 417–438) that are ab-

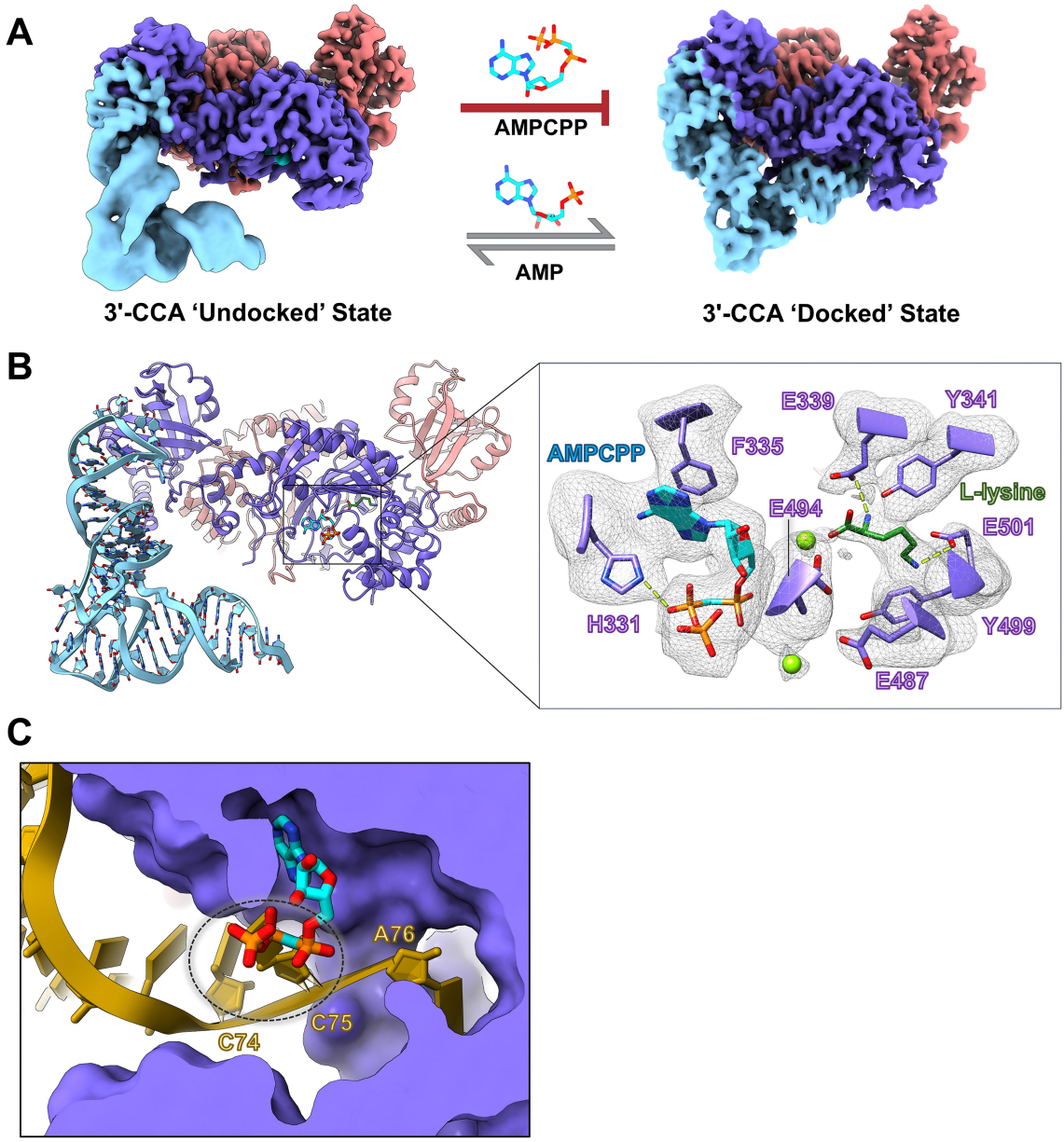

Figure 3. ATP state governs 3′-CCA end docking of tRNA^{Lys3} in the active site. (**A**) Cryo-EM reconstructions of LysRS bound to IVT tRNA^{Lys3} (unmodified) in the presence of L-lysine and either the nonhydrolyzable ATP analog (AMPCPP) (left panel) or the post-hydrolysis ATP analog, AMP (right panel). The AMPCPP bound complex exists solely in the 3′-CCA "undocked" conformation whereas the AMP bound complex can assume the "undocked" and the "docked" conformation. (**B**) Structural model for the AMPCPP bound "undocked" state of the LysRS–tRNA^{Lys3} complex. The right inset shows the interactions of AMPCPP and L-lysine in the active site along with the corresponding cryo-EM map density. (**C**) The docked state of LysRS–tRNA^{Lys3} complex was aligned to the AMPCPP bound "undocked" state. A cross-section view of the LysRS active site is shown highlighting the steric clash between the 3′-CCA end of tRNA^{Lys3} and the β- and γ-phosphate of ATP.

sent in y-AspRS, creating a narrow channel for insertion of the tRNA^{Lys3} 3′-CCA end (Supplementary Fig. S3B and C). Thus, in contrast to AspRS, the two catalytic steps of aminoacylation in LysRS are structurally ordered (Supplementary Movie S3). This ordering may have evolved to prevent conformational states that could act as catalytic dead-ends for the LysRS aminoacylation reaction.

tRNA^{Lys3} modifications are directly recognized by h-LysRS and increase the affinity of the complex

tRNA^{Lys3} is heavily modified in the cell, especially in the loop regions, which alters its overall fold [53] compared to unmodified tRNA^{Lys3}. Comparing the h-LysRS complexes with unmodified IVT tRNA^{Lys3} and modified cellular tRNA^{Lys3} allowed us to dissect the contributions of individual tRNA modifications to h-LysRS binding. A prime example of the crucial role of tRNA^{Lys3} modifications is the selective ordering of the N-terminal extension of h-LysRS in the presence of modified tRNA^{Lys3}. In unmodified tRNA^{Lys3}, U20 and U47 stack against the double-stranded helical core of tRNA^{Lys3}, whereas in cellular tRNA^{Lys3} these bases are modified to D20 and D47, which are nonplanar and assume an unstacked conformation (Fig. 4A). The distance between the N3 atoms of U20 and U47 is ~5 Å in the unmodified tRNA^{Lys3} whereas in modified tRNA^{Lys3}, the distance between D20 and D47 is ~22 Å. This

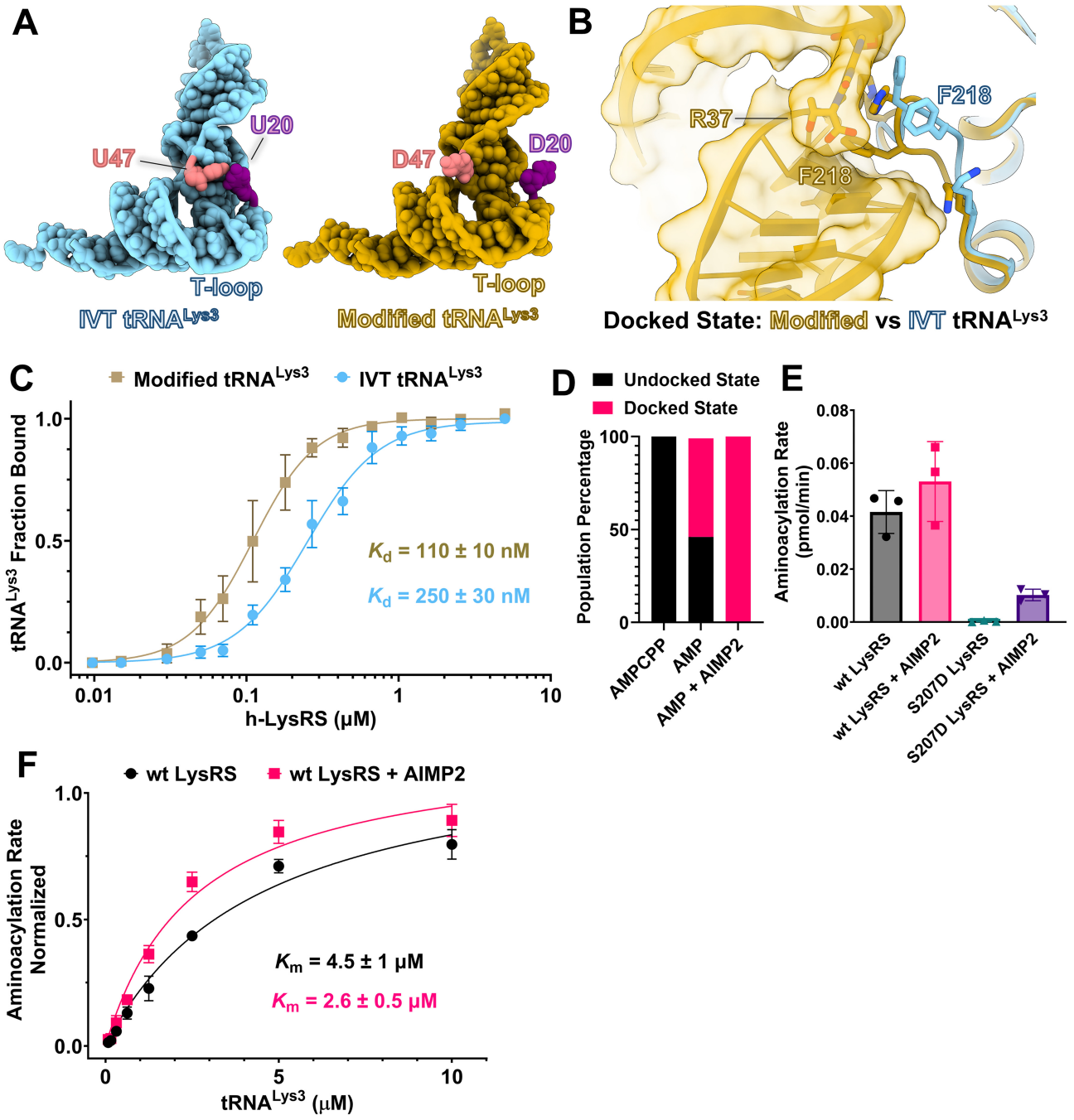

Figure 4. tRNA^{Lys3} modifications and AIMP2 enhance h-LysRS activity. (**A**) Cellular modified tRNA^{Lys3} (gold) and IVT unmodified tRNA^{Lys3} (sky blue) from their respective docked state structures are shown in cartoon representation with the bases shown as spheres. The nucleotide positions 20 (purple) and 47 (coral) in the modified and unmodified tRNA^{Lys3} are highlighted. (**B**) The docked state structures of LysRS with modified tRNA^{Lys3} (gold) and unmodified tRNA^{Lys3} (sky blue) were aligned and a magnified view of the linker region interacting with tRNA^{Lys3} is shown. Modified tRNA^{Lys3} (gold) is shown in surface view and unmodified tRNA^{Lys3} is hidden for clarity. LysRS (gold: modified tRNA^{Lys3} / sky blue: IVT tRNA^{Lys3}) is shown in ribbon view. (**C**) EMSA titrations of h-LysRS binding to unmodified IVT tRNA^{Lys3} and modified tRNA^{Lys3} were carried out in triplicate. Fraction of tRNA^{Lys3} bound by h-LysRS was quantified and the mean is plotted against the protein concentration along with the associated standard error of the mean. The estimated binding affinity (K_d) is denoted along with the associated error from the data fit. (**D**) The percentage of undocked and docked conformational states of the h-LysRS–tRNA^{Lys3} (IVT) complex are shown in bar chart form for the three cryo-EM datasets: h-LysRS–tRNA^{Lys3} in presence of AMPCPP and L-lysine, h-LysRS–tRNA^{Lys3} in presence of AMP and L-lysine, and h-LysRS–tRNALys3–AIMP2–N36 in presence of AMP and L-lysine. (**E**) The initial rates of wt and S207D h-LysRS aminoacylation in the presence and absence of AIMP2–N36 peptide, each measured in triplicate. The mean rates are plotted in bar chart form and error bars represent the associated standard deviation. (**F**) K_m measurement of wt h-LysRS for IVT tRNA^{Lys3} in presence and absence of AIMP2 peptide. The normalized aminoacylation rates are plotted against the tRNA^{Lys3} concentration. Each data point shown is the average of a triplicate measurement and the error bar corresponds to the associated standard deviation.

unstacked conformation of D20 and D47 is not imposed by h-LysRS and is present even in the unbound state of modified tRNA^{Lys3} (Supplementary Fig. S4A). The wider groove created between the D-loop and variable loop by the unstacking of D20 and D47, along with the modified bases in the T-loop of modified tRNA^{Lys3} is crucial for the stable binding of the h-LysRS NTD (Fig. 2A and B, and Supplementary Fig. S4B).

The RNA modifications in the anticodon loop bases, S34 and R37, of cellular modified tRNA^{Lys3} directly interact with h-LysRS. R161 forms ionic interactions with the mcm modification of S34 whereas this interaction is missing for unmodified tRNA^{Lys3} (Supplementary Fig. S4C and Supplementary Movie S2). Similarly, the bulky N6 modification of R37 stacks against H217 and F218, and the ms^2 moiety of R37 packs against H215 of the h-LysRS linker domain. H217 and H215 also form a hydrogen bonding network with the N6-threonyl group and the 5′-phosphate of R37, respectively. For unmodified tRNA^{Lys3}, the h-LysRS linker region (208–220) adopts a significantly different conformation wherein H217 stacks against the A37 base, but H215 and F218 do not participate in tRNA^{Lys3} binding (Fig. 4B). Similarly, the hydrophobic interactions between m^{2}G10 of cellular tRNA^{Lys3} with M212 and P214 of LysRS (Supplementary Fig. S4D) result in a substantially more extensive protein–RNA interface and suggest that the affinity of h-LysRS for modified tRNA^{Lys3} would be higher than that for unmodified tRNA^{Lys3}. Indeed, analyzing the population dynamics from our cryo-EM datasets showed that in the presence of AIMP2–N36 and modified tRNA^{Lys3}, all the LysRS was present in the tRNA^{Lys3}-bound form. In contrast, under identical experimental conditions in the presence of unmodified tRNA^{Lys3}, almost half of the LysRS was found in the apo-state (no tRNA^{Lys3} bound) (Supplementary Fig. S4E and Supplementary Table S5). We carried out EMSAs of h-LysRS with cellular modified tRNA^{Lys3} and IVT unmodified tRNA^{Lys3} to probe the effect of tRNA^{Lys3} modifications on binding affinity. Indeed, EMSA-binding assays confirmed that the affinity of h-LysRS for fully modified tRNA^{Lys3} was ∼2.5-fold higher than for IVT tRNA^{Lys3} (Fig. 4C and Supplementary Fig. S4F).

AIMP2 drives the equilibrium of the h-LysRS–tRNA^{Lys3} complex toward the "docked" state

To understand the effect of AIMP2 binding on the conformational landscape of the LysRS–tRNA^{Lys3} complex, we collected another cryo-EM dataset for the LysRS–tRNA^{Lys3} (IVT) complex in the presence of AMP, L-lysine, and AIMP2–N36 peptide. This dataset yielded two reconstructions: apo-LysRS and LysRS–tRNA^{Lys3} complex. Strikingly, in the presence of AIMP2–N36, all the LysRS–tRNA^{Lys3} complex existed in the "docked" state. For an identical experimental setup, except for the presence of AIMP2, the LysRS–tRNA^{Lys3} complex exhibited an equilibrium between the "docked" (55%) and the "undocked" (45%) states (Fig. 4D and Supplementary Table S5). This indicates that AIMP2 binding allosterically drives the LysRS–tRNA^{Lys3} complex toward the "docked" state, suggesting an active role in enhancing the catalytic efficiency of LysRS.

To test our structure-based predictions that AIMP2 may enhance the aminoacylation activity of LysRS, we carried out aminoacylation assays of LysRS in the absence and presence of AIMP2–N36. Interestingly, AIMP2–N36 was able to rescue the aminoacylation activity in the catalytically inactive S207D mutant of LysRS (Fig. 4E). The presence of AIMP2–N36 also showed a modest increase in the aminoacylation rate of wt LysRS, and despite the rescue effect on the catalytic activity of S207D LysRS, wt LysRS exhibited ∼5-fold higher activity than S207D LysRS. We also measured the K_m of wt LysRS for tRNA^{Lys3} in the absence and presence of AIMP2–N36 and found that in the presence of AIMP2, the K_m of wt LysRS for tRNA^{Lys3} decreased by 2-fold (Fig. 4F). These results corroborate our observations from cryo-EM studies and indicate that AIMP2 and the MSC play an active role in tRNA^{Lys3} aminoacylation by facilitating the transition of the h-LysRS–tRNA^{Lys3} complex toward the "docked" state and enhancing the K_m of h-LysRS for tRNA^{Lys3}.

Discussion

tRNA aminoacylation is a fundamental biological process across all living organisms and AARS are proposed to have been among the first enzymes in the evolutionary timeline [58]. Despite exhibiting a high degree of conservation, the aminoacylation machinery in higher eukaryotes has acquired several additional layers of regulation and complexity over the course of evolution. For example, most prokaryotes carry 20 AARS, one for every aa, but in humans, two distinct sets of AARS are employed for carrying out cytosolic and mitochondrial aminoacylation reactions. Furthermore, almost half of the cytosolic AARS are housed in the MSC where they presumably carry out their canonical aminoacylation function. In humans, AARS also carry out secondary functions in physiological processes ranging from regulation of nuclear transcription to immune responses [59]. Although the simpler bacterial AARS enzymes have been well-characterized, a structural and mechanistic understanding of the more complex aminoacylation machinery in humans and other higher eukaryotes has been lacking.

h-LysRS is an indispensable component of the cellular translation machinery, is a regulator of nuclear transcription [18, 19], and is also a critical host factor for the HIV-1 life cycle [35]. Despite its myriad roles, the structural and mechanistic basis for recognition and aminoacylation of tRNA^{Lys} has been lacking. Furthermore, the roles of the MSC and tRNA modifications in the function of AARS represent fundamental gaps in our understanding of aminoacylation in humans. Our structure of h-LysRS bound to cellular modified tRNA^{Lys3} and a peptide derived from the MSC scaffold protein AIMP2 is the first structure of a human AARS bound to a fully modified cellular tRNA and its MSC interacting partner (Fig. 1B and C).

The tRNA^{Lys3} modifications play an integral role in mediating the specificity of h-LysRS for tRNA^{Lys3}, and directly modulate the structure of the h-LysRS–tRNA^{Lys3} complex (Figs 1 and 2, and Supplementary Fig. S4B–D). The eukaryotic specific NTD of h-LysRS (1-65) folds into an extended helix in the presence of modified tRNA^{Lys3} and forms an extensive interface with the tRNA^{Lys3} acceptor arm, D-loop, variable loop, and T-loop (Fig. 2A). The tRNA^{Lys3} modifications are essential for ordering the h-LysRS NTD, which remains disordered in the presence of unmodified IVT tRNA^{Lys3} (Figs 3A and 5). Previous characterization of rabbit tRNA^{Lys} species identified three major isoforms, designated tRNA^{Lys1}, tRNA^{Lys2}, and tRNA^{Lys3} based on the order in which they eluted from an anion exchange column [22]. The sequence and RNA modifi-

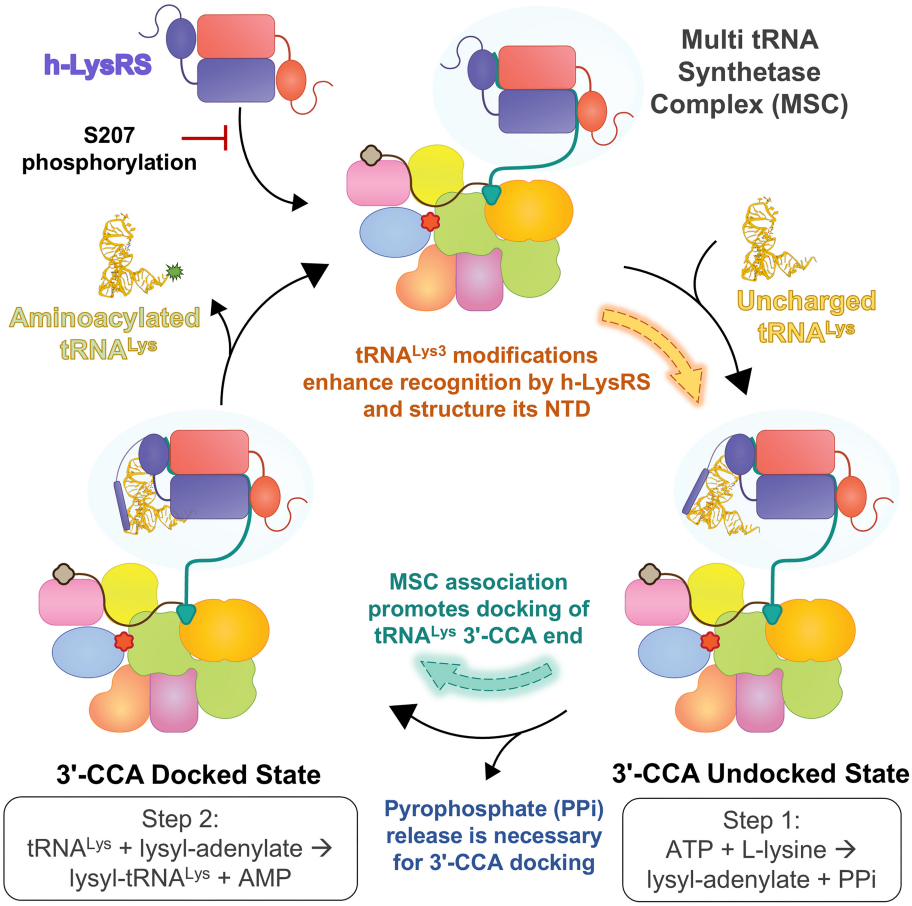

Figure 5. Schematic model for $tRNA^{Lys3}$ aminoacylation and the roles of $tRNA^{Lys3}$ modifications and the MSC in h-LysRS function. h-LysRS associates with the MSC via the scaffold protein AIMP2. Phosphorylation at S207 residue of h-LysRS prevents association with the MSC. h-LysRS selectively binds $tRNA^{Lys}$, and the fidelity of this interaction is imparted by the anticodon loop and the unique $tRNA^{Lys}$ modifications. $tRNA^{Lys}$ modifications are also critical in ordering the h-LysRS NTD into an extended helix that docks at the base of the T-loop and interacts along the length of the anticodon arm. The two catalytic steps in $tRNA^{Lys}$ aminoacylation are structurally ordered by h-LysRS active site. β- and γ-phosphate of the bound ATP creates a steric block and prevents the docking of $tRNA^{Lys}$ 3′-CCA end. In the ATP-bound state, the h-LysRS–$tRNA^{Lys}$ complex exists exclusively in the "3′-CCA undocked" state. Once the ATP hydrolysis catalyzed lysyl–adenylate intermediate is formed and the pyrophosphate (PP_i) by-product is released, $tRNA^{Lys}$ 3′-CCA end can be docked in the active site. In the 3′-CCA docked state, the 3′-A76 nucleotide is unstacked and flipped into the active site, positioning the 3′-hydroxyl of the A76 base for attack on the lysyl–adenylate intermediate. Association with the MSC allosterically drives the equilibrium of the h-LysRS–$tRNA^{Lys}$ complex from the "undocked" state toward the "docked" state, thereby enhancing the catalytic efficiency of h-LysRS. After the completion of the second step in $tRNA^{Lys}$ aminoacylation, aminoacylated $tRNA^{Lys}$ is released along with the byproduct AMP, and the catalytic cycle can begin again.

cations observed in rabbit $tRNA^{Lys3}$ are conserved in human $tRNA^{Lys3}$ investigated here. Comparing the RNA modifications between the three rabbit $tRNA^{Lys}$ isoforms shows that almost all the modifications in the D-loop, variable loop, and T-loop of $tRNA^{Lys3}$ that mediate interaction with h-LysRS are conserved in $tRNA^{Lys1}$ and $tRNA^{Lys2}$. A notable difference between the three isoforms is the lack of S34 modification in $tRNA^{Lys1}$ and $tRNA^{Lys2}$.

Human AspRS and AsnRS, the two other members of the class IIb AARS family, have also evolved an NTD that is absent in their bacterial counterparts. However, whether the NTDs of h-AspRS and h-AsnRS function similarly to h-LysRS remains unresolved due to the lack of sequence conservation in this region (Supplementary Fig. S5A). Alphafold predictions for the secondary structure profile of the NTD of h-LysRS, h-AspRS, and h-AsnRS vary significantly, whereas their ABD domains fold into a highly conserved architecture (Supplementary Fig. S5B). Furthermore, the effect of the unique sequence and RNA modification profiles of $tRNA^{Asp}$ and $tRNA^{Asn}$ on their interactions with h-AspRS and h-AsnRS remains uncharacterized. Further structural studies on h-AspRS and h-AsnRS are needed to understand the roles of their respective NTDs and identify commonalities across the class IIb family of cytosolic AARS. Recently, the human mitochondrial tRNA maturation pathway was structurally characterized [60], and it revealed that the mitochondrial tRNA methyltransferase 10C (TRMT10C) employs an extended α-helical motif that is remarkably similar to h-LysRS NTD in its charge distribution and interaction network with tRNA. This suggests that the h-LysRS NTD may be a conserved interaction motif in metazoan tRNA-binding proteins.

The evolutionary advantage of housing cytosolic AARS in the MSC has been unclear and several potential functions have been proposed for the MSC [14, 61]. h-LysRS association with the MSC has been proposed to protect the aminoacylation function by preventing modification and/or recruitment into alternate cellular pathways [62]. Herein, we show that the association of h-LysRS with the MSC via the scaffold protein AIMP2 enhances the aminoacylation efficiency of $tRNA^{Lys3}$ (Figs 1 and 4). AIMP2 allosterically modulates the equilib-

rium of the h-LysRS–tRNA^{Lys3} complex toward the "docked" state (Fig. 5). Whether an association with the MSC enhances the catalytic activity of other AARS remains to be explored.

Aminoacylation by all AARS is a two-step catalytic reaction, wherein the cognate aa is first activated using ATP hydrolysis to generate the aminoacyl–adenylate intermediate and then the activated aa is conjugated to the 3′-end of the respective tRNA (2′-hydroxyl for class I AARS and 3′-hydroxyl for class II AARS). These two catalytic steps in tRNA^{Lys3} aminoacylation are sequentially ordered by the LysRS active site such that the docking of the tRNA^{Lys3} 3′-CCA end in the active site can only occur after ATP hydrolysis driven activation of L-lysine is completed (Fig. 3 and Supplementary Fig. S6). This is in contrast to the closely related AspRS, wherein the active site can simultaneously bind ATP, L-aspartic acid, and the 3′-CCA end of tRNA^{Asp} (Supplementary Fig. S3). This stems from the differences in the active site architecture wherein insertions between motifs 2 and 3 of h-LysRS lead to an active site entrance that is much narrower than AspRS and incompatible with simultaneous binding of ATP and the 3′-CCA end of tRNA^{Lys3}. AsnRS is believed to have evolved from AspRS [63], and its active site is more similar to AspRS than LysRS, suggesting that the two catalytic steps in tRNA^{Asn} aminoacylation are likely not ordered.

Recently, several neurological and metabolic disorders have been linked to dysregulation of tRNA modifications, collectively referred to as tRNA modopathies [64]. For example, several tRNA^{Lys3} modopathies including microcephaly [65], nephropathy [66], diabetes [67], and cancer [68] are linked to the downregulation of the S34 and R37 modifications. The exact mechanistic basis for how changes in the tRNA modification landscape lead to these disorders remains unclear and understudied. Our results herein show the critical role of tRNA^{Lys3} modifications in mediating the specificity of h-LysRS–tRNA^{Lys3} interaction and predict that downregulation of these modifications, although not essential for *in vitro* tRNA binding and aminoacylation, would likely impair the aminoacylation efficiency of tRNA^{Lys} in cells, which may impact the translation of lysine-rich proteins. Modifications may also provide a fitness advantage under certain environmental conditions including cellular stress [69, 70]. The significant structural rearrangements observed with modified tRNA^{Lys3} bound to LysRS may finetune the translation machinery under specific cellular conditions. For example, during T-cell activation, ms^2t^6A37 in the anticodon loop of tRNA^{Lys3} showed dynamic changes with an impact on frameshifting [71].

In summary, our results provide an in-depth understanding of tRNA^{Lys3} recognition and aminoacylation by h-LysRS and delineate the critical roles of tRNA^{Lys3} modifications and the MSC in h-LysRS function. The structural and mechanistic insights presented herein provide a strong foundation for future work aimed at understanding the aminoacylation machinery in humans as well as the increasing number of neurological and metabolic disorders linked to defects in the human aminoacylation and tRNA modification machinery [4, 28–30].

Acknowledgements

Author contributions: S.C.D., K.M.-F., and Y.X. conceptualized and designed the study; S.C.D. carried out the cryo-EM sample preparation, data collection, data processing, and model building; C.P. and A.K. purified the cellular modified tRNA^{Lys3}. S.C.D. and C.R.B. purified the wt and S207D LysRS. C.R.B. carried out the aminoacylation assays and EMSAs. C.H. and P.A.L. carried out the LC-MS validation and analysis. S.C.D., Y.X., and K.M.-F. wrote the original draft of the manuscript. All authors contributed to review and editing.

Supplementary data

Supplementary data is available at NAR online.

Conflict of interest

None declared.

Funding

We would like to acknowledge the Laboratory for BioMolecular Structure (LBMS) at Brookhaven National Laboratory, supported by the DOE Office of Biological and Environmental Research (KP1607011) for access to Krios cryo-EM. This work was funded by the National Institutes of Health (NIH) grants R21 AI157890 (to Y.X.), NIH GM058853 (to P.A.L.), T32 GM141955 (to C.R.B.), R35 GM141880, and R01 AI150493 (to K.M.-F.).

Data availability

The coordinates and cryo-EM density maps for all the structures reported here have been deposited in the PDB and EMDB, respectively. The accession codes are as follows: h-LysRS-AIMP2-modified tRNA^{Lys3} (Docked State, AMP bound) complex (PDB: 9DPL, EMD-47106); h-LysRS-IVT tRNA^{Lys3} (Undocked State, AMPCPP bound) complex (PDB: 9DPB, EMD-47101); h-LysRS-IVT tRNA^{Lys3} (Undocked State, AMP bound) complex (PDB: 9DOW/EMD-47094); and h-LysRS-IVT tRNA^{Lys3} (Docked State, AMP bound) complex (PDB: 9DPA, EMD-47100). Plasmids and cell lines used in this study are available upon request. Any further information and requests for resources should be directed to and will be fulfilled by S.C.D. (swapnilchandrakant.devarkar@yale.edu).

References

1. Hoagland MB, Stephenson ML, Scott JF *et al.* A soluble ribonucleic acid intermediate in protein synthesis. *J Biol Chem* 1958;**231**:241–57. https://doi.org/10.1016/S0021-9258(19)77302-5
2. Hoagland MB, Keller EB, Zamecnik PC. Enzymatic carboxyl activation of amino acids. *J Biol Chem* 1956;**218**:345–58. https://doi.org/10.1016/S0021-9258(18)65898-3
3. Woese CR, Olsen GJ, Ibba M *et al.* Aminoacyl-tRNA synthetases, the genetic code, and the evolutionary process. *Microbiol Mol Biol Rev* 2000;**64**:202–36. https://doi.org/10.1128/MMBR.64.1.202-236.2000
4. Antonellis A, Green ED. The role of aminoacyl-tRNA synthetases in genetic diseases. *Annu Rev Genom Hum Genet* 2008;**9**:87–107. https://doi.org/10.1146/annurev.genom.9.081307.164204
5. Tolkunova E, Park H, Xia J *et al.* The human lysyl-tRNA synthetase gene encodes both the cytoplasmic and mitochondrial enzymes by means of an unusual alternative splicing of the primary transcript. *J Biol Chem* 2000;**275**:35063–9. https://doi.org/10.1074/jbc.M006265200
6. Mudge SJ, Williams JH, Eyre HJ *et al.* Complex organisation of the 5′-end of the human glycine tRNA synthetase gene. *Gene*

1998;**209**:45–50. https://doi.org/10.1016/S0378-1119(98)00007-9
7. Alexandrova J, Paulus C, Rudinger-Thirion J *et al.* Elaborate uORF/IRES features control expression and localization of human glycyl-tRNA synthetase. *RNA Biol* 2015;**12**:1301–13. https://doi.org/10.1080/15476286.2015.1086866
8. Yaremchuk AD, Krikliviy IA, Cusack S *et al.* Cocrystallization of lysyl-tRNA synthetase from *Thermus thermophilus* with its cognate tRNAlys and with *Escherichia coli* tRNAlys. *Proteins* 1995;**21**:261–4. https://doi.org/10.1002/prot.340210309
9. Guo M, Ignatov M, Musier-Forsyth K *et al.* Crystal structure of tetrameric form of human lysyl-tRNA synthetase: implications for multisynthetase complex formation. *Proc Natl Acad Sci USA* 2008;**105**:2331–6. https://doi.org/10.1073/pnas.0712072105
10. Cusack S, Hartlein M, Leberman R. Sequence, structural and evolutionary relationships between class 2 aminoacyl-tRNA synthetases. *Nucl Acids Res* 1991;**19**:3489–98. https://doi.org/10.1093/nar/19.13.3489
11. Francin M, Kaminska M, Kerjan P *et al.* The N-terminal domain of mammalian lysyl-tRNA synthetase is a functional tRNA-binding domain. *J Biol Chem* 2002;**277**:1762–9. https://doi.org/10.1074/jbc.M109759200
12. Mirande M, Le Corre D, Waller JP. A complex from cultured Chinese hamster ovary cells containing nine aminoacyl-tRNA synthetases. Thermolabile leucyl-tRNA synthetase from the tsH1 mutant cell line is an integral component of this complex. *Eur J Biochem* 1985;**147**:281–9. https://doi.org/10.1111/j.1432-1033.1985.tb08748.x
13. Cerini C, Kerjan P, Astier M *et al.* A component of the multisynthetase complex is a multifunctional aminoacyl-tRNA synthetase. *EMBO J* 1991;**10**:4267–77. https://doi.org/10.1002/j.1460-2075.1991.tb05005.x
14. Hyeon DY, Kim JH, Ahn TJ *et al.* Evolution of the multi-tRNA synthetase complex and its role in cancer. *J Biol Chem* 2019;**294**:5340–51. https://doi.org/10.1074/jbc.REV118.002958
15. Khan K, Baleanu-Gogonea C, Willard B *et al.* 3-Dimensional architecture of the human multi-tRNA synthetase complex. *Nucleic Acids Res* 2020;**48**:8740–54. https://doi.org/10.1093/nar/gkaa569
16. Ofir-Birin Y, Fang P, Bennett SP *et al.* Structural switch of lysyl-tRNA synthetase between translation and transcription. *Mol Cell* 2013;**49**:30–42. https://doi.org/10.1016/j.molcel.2012.10.010
17. Duchon AA, St Gelais C, Titkemeier N *et al.* HIV-1 exploits a dynamic multi-aminoacyl-tRNA synthetase complex to enhance viral replication. *J Virol* 2017;**91**:01240. https://doi.org/10.1128/JVI.01240-17
18. Yannay-Cohen N, Carmi-Levy I, Kay G *et al.* LysRS serves as a key signaling molecule in the immune response by regulating gene expression. *Mol Cell* 2009;**34**:603–11. https://doi.org/10.1016/j.molcel.2009.05.019
19. Tang Y, Behrens RT, St Gelais C *et al.* Human lysyl-tRNA synthetase phosphorylation promotes HIV-1 proviral DNA transcription. *Nucleic Acids Res* 2023;**51**:12111–23. https://doi.org/10.1093/nar/gkad941
20. Jackman JE, Alfonzo JD. Transfer RNA modifications: nature's combinatorial chemistry playground. *WIREs RNA* 2013;**4**:35–48. https://doi.org/10.1002/wrna.1144
21. Ganesh RB, Maerkl SJ. Biochemistry of aminoacyl tRNA synthetase and tRNAs and their engineering for cell-free and synthetic cell applications. *Front Bioeng Biotechnol* 2022;**10**:918659. https://doi.org/10.3389/fbioe.2022.918659
22. Raba M, Limburg K, Burghagen M *et al.* Nucleotide sequence of three isoaccepting lysine tRNAs from rabbit liver and SV40-transformed mouse fibroblasts. *Eur J Biochem* 1979;**97**:305–18. https://doi.org/10.1111/j.1432-1033.1979.tb13115.x
23. Durant PC, Bajji AC, Sundaram M *et al.* Structural effects of hypermodified nucleosides in the Escherichia coli and human tRNALys anticodon loop: the effect of nucleosides s2U, mcm5U, mcm5s2U, mnm5s2U, t6A, and ms2t6A. *Biochemistry* 2005;**44**:8078–89. https://doi.org/10.1021/bi050343f
24. Atkins JF, Loughran G, Bhatt PR *et al.* Ribosomal frameshifting and transcriptional slippage: from genetic steganography and cryptography to adventitious use. *Nucleic Acids Res* 2016;**44**:7007–78.
25. Sundaram M, Durant PC, Davis DR. Hypermodified nucleosides in the anticodon of tRNALys stabilize a canonical U-turn structure. *Biochemistry* 2000;**39**:12575–84. https://doi.org/10.1021/bi0014655
26. Helm M. Post-transcriptional nucleotide modification and alternative folding of RNA. *Nucleic Acids Res* 2006;**34**:721–33. https://doi.org/10.1093/nar/gkj471
27. Biela A, Hammermeister A, Kaczmarczyk I *et al.* The diverse structural modes of tRNA binding and recognition. *J Biol Chem* 2023;**299**:104966. https://doi.org/10.1016/j.jbc.2023.104966
28. Turvey AK, Horvath GA, Cavalcanti ARO. Aminoacyl-tRNA synthetases in human health and disease. *Front Physiol* 2022;**13**:1029218. https://doi.org/10.3389/fphys.2022.1029218
29. Burgess RW, Storkebaum E. tRNA dysregulation in neurodevelopmental and neurodegenerative diseases. *Annu Rev Cell Dev Biol* 2023;**39**:223–52. https://doi.org/10.1146/annurev-cellbio-021623-124009
30. Jiang L, Jones J, Yang XL. Human diseases linked to cytoplasmic aminoacyl-tRNA synthetases. *Enzymes* 2020;**48**:277–319. https://doi.org/10.1016/bs.enz.2020.06.009
31. McLaughlin HM, Sakaguchi R, Liu C *et al.* Compound heterozygosity for loss-of-function lysyl-tRNA synthetase mutations in a patient with peripheral neuropathy. *Am Hum Genet* 2010;**87**:560–6. https://doi.org/10.1016/j.ajhg.2010.09.008
32. Zhou XL, He LX, Yu LJ *et al.* Mutations in KARS cause early-onset hearing loss and leukoencephalopathy: potential pathogenic mechanism. *Hum Mutat* 2017;**38**:1740–50. https://doi.org/10.1002/humu.23335
33. Wei FY, Suzuki T, Watanabe S *et al.* Deficit of tRNA (Lys) modification by Cdkal1 causes the development of type 2 diabetes in mice. *J Clin Invest* 2011;**121**:3598–608. https://doi.org/10.1172/JCI58056
34. Arrondel C, Missoury S, Snoek R *et al.* Defects in t (6)A tRNA modification due to GON7 and YRDC mutations lead to Galloway–Mowat syndrome. *Nat Commun* 2019;**10**:3967. https://doi.org/10.1038/s41467-019-11951-x
35. Jin D, Musier-Forsyth K. Role of host tRNAs and aminoacyl-tRNA synthetases in retroviral replication. *J Biol Chem* 2019;**294**:5352–64. https://doi.org/10.1074/jbc.REV118.002957
36. Liu S, Comandur R, Jones CP *et al.* Anticodon-like binding of the HIV-1 tRNA-like element to human lysyl-tRNA synthetase. *RNA* 2016;**22**:1828–35. https://doi.org/10.1261/rna.058081.116
37. Cusack S, Yaremchuk A, Tukalo M. The crystal structures of *T. thermophilus* lysyl-tRNA synthetase complexed with E. coli tRNA (Lys) and a *T. thermophilus* tRNA (Lys) transcript: anticodon recognition and conformational changes upon binding of a lysyl-adenylate analogue. *EMBO J* 1996;**15**:6321–34. https://doi.org/10.1002/j.1460-2075.1996.tb01022.x
38. Drino A, Oberbauer V, Troger C *et al.* Production and purification of endogenously modified tRNA-derived small RNAs. *RNA Biol* 2020;**17**:1104–15. https://doi.org/10.1080/15476286.2020.1733798
39. Lobue PA, Yu N, Jora M *et al.* Improved application of RNAModMapper—an RNA modification mapping software tool - for analysis of liquid chromatography tandem mass spectrometry (LC-MS/MS) data. *Methods* 2019;**156**:128–38. https://doi.org/10.1016/j.ymeth.2018.10.012
40. Yu N, Lobue PA, Cao X *et al.* RNAModMapper: RNA modification mapping software for analysis of liquid chromatography tandem mass spectrometry data. *Anal Chem* 2017;**89**:10744–52. https://doi.org/10.1021/acs.analchem.7b01780

41. Milligan JF, Groebe DR, Witherell GW *et al.* Oligoribonucleotide synthesis using T7 RNA polymerase and synthetic DNA templates. *Nucl Acids Res* 1987;**15**:8783–98. https://doi.org/10.1093/nar/15.21.8783
42. Chillón I, Marcia M, Legiewicz M *et al.* Native purification and analysis of long RNAs. *Methods Enzymol* 2015;**558**:3–37. https://doi.org/10.1016/bs.mie.2015.01.008
43. Cantara WA, Pathirage C, Hatterschide J *et al.* Phosphomimetic S207D lysyl-tRNA synthetase binds HIV-1 5′UTR in an open conformation and increases RNA dynamics. *Viruses* 2022;**14**:1556. https://doi.org/10.3390/v14071556
44. Brunelle JL, Green R. In vitro transcription from plasmid or PCR-amplified DNA. *Methods Enzymol* 2013;**530**:101–14. https://doi.org/10.1016/B978-0-12-420037-1.00005-1
45. Kavoor A, Kelly P, Ibba M. *Escherichia coli* alanyl-tRNA synthetase maintains proofreading activity and translational accuracy under oxidative stress. *J Biol Chem* 2022;**298**:101601. https://doi.org/10.1016/j.jbc.2022.101601
46. Han NC, Bullwinkle TJ, Loeb KF *et al.* The mechanism of β-N-methylamino-l-alanine inhibition of tRNA aminoacylation and its impact on misincorporation. *J Biol Chem* 2020;**295**:1402–10. https://doi.org/10.1016/S0021-9258(17)49898-X
47. Punjani A, Rubinstein JL, Fleet DJ *et al.* cryoSPARC: algorithms for rapid unsupervised cryo-EM structure determination. *Nat Methods* 2017;**14**:290–6. https://doi.org/10.1038/nmeth.4169
48. Emsley P, Lohkamp B, Scott WG *et al.* Features and development of Coot. *Acta Crystallogr D Biol Crystallogr* 2010;**66**:486–501. https://doi.org/10.1107/S0907444910007493
49. Liebschner D, Afonine PV, Baker ML *et al.* Macromolecular structure determination using X-rays, neutrons and electrons: recent developments in Phenix. *Acta Crystallogr D Struct Biol* 2019;**75**:861–77. https://doi.org/10.1107/S2059798319011471
50. Ryder SP, Recht MI, Williamson JR. 2008; In Lin R-J (ed.), *RNA-Protein Interaction Protocols*. Totowa, NJ: Humana Press, 99–115.
51. Arnez JG, Steitz TA. Crystal structure of unmodified tRNA (Gln) complexed with glutaminyl-tRNA synthetase and ATP suggests a possible role for pseudo-uridines in stabilization of RNA structure. *Biochemistry* 1994;**33**:7560–7. https://doi.org/10.1021/bi00190a008
52. Vogele J, Duchardt-Ferner E, Kruse H *et al.* Structural and dynamic effects of pseudouridine modifications on noncanonical interactions in RNA. *RNA* 2023;**29**:790–807. https://doi.org/10.1261/rna.079506.122
53. Benas P, Bec G, Keith G *et al.* The crystal structure of HIV reverse-transcription primer tRNA (Lys,3) shows a canonical anticodon loop. *RNA* 2000;**6**:1347–55. https://doi.org/10.1017/S1355838200000911
54. Liu S, Refaei M, Liu S *et al.* Hairpin RNA-induced conformational change of a eukaryotic-specific lysyl-tRNA synthetase extension and role of adjacent anticodon-binding domain. *J Biol Chem* 2020;**295**:12071–85. https://doi.org/10.1074/jbc.RA120.013852
55. Shiba K, Stello T, Motegi H *et al.* Human lysyl-tRNA synthetase accepts nucleotide 73 variants and rescues *Escherichia coli* double-defective mutant. *J Biol Chem* 1997;**272**:22809–16. https://doi.org/10.1074/jbc.272.36.22809
56. Cavarelli J, Eriani G, Rees B *et al.* The active site of yeast aspartyl-tRNA synthetase: structural and functional aspects of the aminoacylation reaction. *EMBO J* 1994;**13**:327–37. https://doi.org/10.1002/j.1460-2075.1994.tb06265.x
57. Kaiser F, Bittrich S, Salentin S *et al.* Backbone brackets and arginine tweezers delineate class I and class II aminoacyl tRNA synthetases. *PLoS Comput Biol* 2018;**14**:e1006101. https://doi.org/10.1371/journal.pcbi.1006101
58. Rubio Gomez MA, Ibba M. Aminoacyl-tRNA synthetases. *RNA* 2020;**26**:910–36. https://doi.org/10.1261/rna.071720.119
59. Sun L, Zhou XL, Zhou ZW *et al.* Editorial: noncanonical functions of aminoacyl-tRNA synthetases. *Front Physiol* 2023;**14**:1165515. https://doi.org/10.3389/fphys.2023.1165515
60. Meynier V, Hardwick SW, Catala M *et al.* Structural basis for human mitochondrial tRNA maturation. *Nat Commun* 2024;**15**:4683. https://doi.org/10.1038/s41467-024-49132-0
61. Cui H, Kapur M, Diedrich JK *et al.* Regulation of ex-translational activities is the primary function of the multi-tRNA synthetase complex. *Nucleic Acids Res* 2021;**49**:3603–16. https://doi.org/10.1093/nar/gkaa1183
62. Wu S, Zheng L, Hei Z *et al.* Human lysyl-tRNA synthetase evolves a dynamic structure that can be stabilized by forming complex. *Cell Mol Life Sci* 2022;**79**:128. https://doi.org/10.1007/s00018-022-04158-9
63. Shiba K, Motegi H, Yoshida M *et al.* Human asparaginyl-tRNA synthetase: molecular cloning and the inference of the evolutionary history of asx-tRNA synthetase family. *Nucleic Acids Res* 1998;**26**:5045–51. https://doi.org/10.1093/nar/26.22.5045
64. Chujo T, Tomizawa K. Human transfer RNA modopathies: diseases caused by aberrations in transfer RNA modifications. *FEBS J* 2021;**288**:7096–122. https://doi.org/10.1111/febs.15736
65. Shaheen R, Mark P, Prevost CT *et al.* Biallelic variants in CTU2 cause DREAM-PL syndrome and impair thiolation of tRNA wobble U34. *Hum Mutat* 2019;**40**:2108–20. https://doi.org/10.1002/humu.23870
66. Braun DA, Rao J, Mollet G *et al.* Mutations in KEOPS-complex genes cause nephrotic syndrome with primary microcephaly. *Nat Genet* 2017;**49**:1529–38. https://doi.org/10.1038/ng.3933
67. Steinthorsdottir V, Thorleifsson G, Reynisdottir I *et al.* A variant in CDKAL1 influences insulin response and risk of type 2 diabetes. *Nat Genet* 2007;**39**:770–5. https://doi.org/10.1038/ng2043
68. Delaunay S, Rapino F, Tharun L *et al.* Elp3 links tRNA modification to IRES-dependent translation of LEF1 to sustain metastasis in breast cancer. *J Exp Med* 2016;**213**:2503–23. https://doi.org/10.1084/jem.20160397
69. Gu C, Begley TJ, Dedon PC. tRNA modifications regulate translation during cellular stress. *FEBS Lett* 2014;**588**:4287–96. https://doi.org/10.1016/j.febslet.2014.09.038
70. Pan T. Modifications and functional genomics of human transfer RNA. *Cell Res* 2018;**28**:395–404. https://doi.org/10.1038/s41422-018-0013-y
71. Rak R, Polonsky M, Eizenberg-Magar I *et al.* Dynamic changes in tRNA modifications and abundance during T cell activation. *Proc Natl Acad Sci USA* 2021;**118**:e2106556118. https://doi.org/10.1073/pnas.2106556118

Received: December 2, 2024. **Revised:** February 1, 2025. **Editorial Decision:** February 3, 2025. **Accepted:** February 6, 2025